Nanoscale Advances

Accepted Manuscript

This article can be cited before page numbers have been issued, to do this please use: B. Vasic, L. Balcells, N. Mestres Andreu, B. Martinez, A. Pomar and Z. Konstantinovic, *Nanoscale Adv.*, 2026, DOI: 10.1039/D6NA00067C.

ROYAL SOCIETY OF CHEMISTRY

rsc.li/nanoscale-advances

View Article Online
DOI: 10.1039/D6NA00067C

ARTICLE

Evidence of dipolar magnetic interactions in the self-assembly of two-dimensional magnetic nanocubes

Received 00th January 20xx,
Accepted 00th January 20xx

DOI: 10.1039/x0xx00000x

Borislav Vasić,*[a] Lluis Balcells [b], Narcis Mestres[b], Benjamin Martínez[b], Alberto Pomar*[b] and Zorica Konstantinović*[a]

We report an experimental study on the self-assembly and atomic force microscopy (AFM) manipulation of ligand-free Fe/Fe_3O_4 nanocubes synthesized via a gas aggregation cluster source, a method that eliminates steric and capillary effects typical of wet-chemistry routes. This approach isolates magnetic dipolar and surface forces as the primary drivers of cluster formation. Sub-20 nm nanocubes spontaneously organize into close-packed two-dimensional arrays with dominant {100}–{100} contacts, exhibiting a preferential [001] magnetic easy axis consistent with Fe-core-driven anisotropy. AFM manipulation reveals elastic-like responses in monolayers, strong shape persistence of compact clusters, and shear-induced reorganization into short chains with defined orientations. Mobility is strongly layer-dependent, with multilayers requiring significantly higher loads to initiate motion. By mapping local lateral-force peaks during manipulation and estimating the relevant force scales, it is shown that magnetic dipolar interactions act together with van der Waals attraction and frictional dissipation to restrict particle motion. These findings contribute to a better understanding of self-assembly and shear-assisting assembly of magnetic nanoparticles and suggest that magnetic nanocubes may serve as versatile building blocks for two- and three-dimensional magnetic architectures.

1. Introduction

Self-assembly of nanoscale building blocks offers a scalable, low-cost alternative to top-down lithography for creating functional architectures with tailored properties. The ability to assemble nanoscopic components through a bottom-up approach into desired patterns with specific functional properties has enormous technological relevance.[1,2,3,4] In many multicomponent systems, the resulting patterns encode the underlying interactions through the shape and surface chemistry of the constituents.[5,6,7] Among these, magnetic nanoparticles are of particular interest for sensing, data storage, catalysis, and biomedicine, where controlled arrangement translates directly into performance.[8,9,10,11] For magnetic colloids, the assembly pathway reflects a competition among forces of comparable magnitude—van der Waals, Coulombic, dipolar magnetic, and substrate-mediated interactions—and can be tuned through particle size and shape.[6]

In particular, cuboidal particles (nanocubes) are especially attractive since their faceted geometry restricts attachment orientations and promotes high packing density and strong face–face contacts, enabling mesoscale structures with enhanced adhesion and surface area (higher surface to volume ratio compared to spheroids).[12,5] On the other hand, the size of nanocubes offers an additional degree of freedom for tailoring magnetic properties, as a magnetic configuration of constitutive single domain elements is not determined exclusively by the magnetic bulk properties but also shows important dependence on nanocube size. For instance, in iron-based core/shell nanocubes, the balance between the Fe core and Fe_3O_4 shell controls magnetic anisotropy; consequently, the preferred magnetization axes—and thus interparticle alignment—depend sensitively on cube size and core/shell ratio.[13,14] Consequently, the magnetic anisotropy determines a way of assembling low-dimensional magnetic nanostructures, as nanocubes , via the subtle balance between magnetic dipolar interaction and surface forces.[15,16,17,18] This sensitivity opens a route to encode assembly rules via anisotropy, allowing formation of 1D chains[17,19,20], 2D clusters[10,21] to 3D structures.[5]

Beyond spontaneous self-assembly, atomic force microscopy (AFM) manipulation provides nanoscale control over particle arrangement and a direct probe of tip–sample mechanics and lateral forces.[22,23,24,25] While this technique has been widely used to study friction[26,27], sliding anisotropy[28,29,30], adhesion[31], and electrostatics[32], AFM manipulation of magnetic nanoparticles remains sparsely explored and only in context of

[a] Center for Solid State Physics and New Materials, Institute of Physics Belgrade, University of Belgrade, Pregrevica 118, 11080 Belgrade, Serbia.
[b] Institut de Ciencia de Materials de Barcelona, ICMAB-CSIC, Campus de la UAB, 08193 Bellaterra, Spain

*Corresponding authors. E-mail addresses: bvasic@ipb.ac.rs (B. Vasić), alberto.pomar@csic.es (A. Pomar) and zorica.konstantinovic@ipb.ac.rs (Z. Konstantinović)
Supplementary Information available: See DOI: 10.1039/x0xx00000x

their lateral movement.[33,34,35,36,37] On the other hand, interactions between magnetic nanoparticles manipulated by AFM tip especially with a focus on their mutual interactions and collective mechanical response under shear have not been explored at all. Addressing this gap is essential for designing robust magnetic assemblies and for developing shear-field-assisted fabrication strategies.

This study explores iron/iron oxide (Fe/Fe_3O_4) nanocubes assemble via magnetic dipolar interactions and their manipulation using AFM. Nanocubes in sub-20 nm range are produced by a gas aggregation cluster source, a dry synthesis route that provides ligand-free particles with clean interfaces. As a result, steric and capillary effects common in wet-chemistry methods are absent, allowing a clear investigation of the roles of magnetic dipolar and surface forces in "lego"-type clustering. Several experimental techniques including electron microscopies, SQUID magnetometry, contact-mode AFM manipulation and lateral-force mapping are combined to analyze the assembly behavior. The study quantifies assembly as a function of surface coverage, tracking the evolution from isolated nanocubes and small aggregates to close-packed, mainly two-dimensional "lego"-like clusters and, at the highest coverages, three-dimensional agglomerates. It identifies dominant face–face ({100}–{100}) contacts between particles and infers a preferred magnetic easy axis in sub-20 nm cubes, consistent with a thin magnetite shell and an iron-core-dominated magnetic anisotropy. The influence of applied shear forces on nanoparticle rearrangement, enabling shear-induced alignment, is explored in single layer "lego" clusters (2D) as well as in multiple layers of magnetic nanocubes (3D), giving access to the overall macroscopic properties of the assembly.

This work introduces the use of ligand-free Fe/Fe_3O_4 nanocubes produced by a gas-phase method to isolate intrinsic magnetic and surface interactions, revealing how dipolar coupling and anisotropy govern "lego-like" self-assembly into ordered structures. It further provides the first systematic study of AFM tip-induced interactions and collective mechanical behavior of magnetic nanoparticles, demonstrating that shear can actively drive reversible reconfiguration, alignment, and chain formation while maintaining mechanical stability without organic ligands. Overall, it establishes a new framework for shear-assisted, programmable assembly of robust, reconfigurable magnetic nanostructures.

2. Experimental

2.1. Cluster gun preparation

Iron nanoparticles (NP) have been grown in a home built cluster source connected to the vacuum system with base pressure in 10^{-6} Torr range. A cluster gun provides pre-formed separate nanoparticles which organize in disordered structure while the characteristics of individual nanoparticles (size, shape) can be controlled by growth conditions. Previously, it was found that nanoparticles size depends on various parameters, such as cluster gun power, Ar gas flow, nanoparticle traveling distance.[17] In the present case, DC magnetron (1 inch) with a Fe target (99.95% purity) was operated typically at the cluster gun power of 30 W. Nanoparticles in the range of 15-20 nm are prepared at fixed travel distance of d= 7 cm and fixed 80 cm^3/min Ar gas flow and pressures in the low 10^{-3} Torr range. No mass quadrupole, that allow the selection of nanoparticle size, has been used in the present work. Different NP concentrations are obtained using different deposition time (2-240 s). Fe-based nanoparticles are deposited on silica substrates for scanning electron microscopy (SEM) observation as well as magnetic characterisation and AFM manipulation, while for transmission electron microscopy (TEM) experiments, special TEM carbon-coated grids were used.

2.2. Structural and magnetic characterisation

The self-assembly of nanoparticle was analysed by SEM using a QUANTA FEI 200 FEG-ESEM microscope. The core-shell structure of Fe/Fe_3O_4 nanoparticles (crystallinity, morphology, and size) was examined by TEM using a JEOL JEM 1210 operating at 120 KV. The particle-size characteristics has been reported previously in [8], while the statistics of core-shell structures in the range of nanoparticle size (15-20 nm) can be find in [17].

Magnetic characterization of the sample with high nanoparticle concentration was performed by using a Quantum Design MPMS-2 SQUID magnetometer, in the ±50 kOe magnetic field range, at room temperature (RT).

2.3. Atomic force microscopy manipulation

AFM measurements were conducted using an NT-MDT Ntegra Prima system. Manipulations were performed via raster scanning in contact mode. In such experiments, the AFM tip pushes nanoparticles laterally along the substrate toward desired locations. The normal force applied by the AFM tip served as the key parameter to control tip-sample mechanical interaction. By adjusting the normal load, we were able to regulate the mechanical shear forces exerted on the nanocubes. The scan velocity during manipulation was on the order of 1 µm/s. Although all manipulations employed raster scanning, we varied the width of the scan area along the slow scan axis. This allowed us to adjust the manipulation regions from square areas of 1 × 1 µm² to narrow horizontal stripes of 1 × 0.1 µm².

During manipulation processes, both topographic (height) and lateral force signals were recorded. The lateral force signal, which corresponds to the torsional deflection of the AFM cantilever, provides additional insights into tip–sample interactions during lateral displacement of the nanocubes. The final lateral force was determined as half the difference between the corresponding force signals recorded during the forward (trace) and backward (retrace) scan directions. Lateral force calibration was performed using the standard wedge calibration method.[38]

AFM manipulations were performed using soft CSG01 probes from NT-MDT (typical force constant of 0.03 N/m) and stiffer AC240TS probes from Asylum (typical force constant of 2 N/m). In the former case, scanning was carried out exclusively in contact mode. In contrast, the use of stiffer probes enabled

switching between contact and tapping modes. Consequently, for this configuration, imaging before and after manipulation was conducted in tapping mode, while AFM manipulations themselves were performed in contact mode. Tapping-mode imaging is more suitable for nanoparticle systems, due to significantly lower lateral forces compared to contact mode. As a result, tapping-mode measurements offer more reliable imaging of nanoparticles by minimizing unintended lateral displacements. Stiffer probes were employed for the measurements presented in Figs. 4, 5, 7, and 8, while softer probes were used for Fig. 6. With stiffer probes, higher normal loads were applied to generate AFM-induced shear forces sufficient to induce lateral displacement of the nanocubes. In contrast, softer probes were used at lower normal loads to achieve only slight rearrangement of the nanocubes into oriented chains.

3. Results and discussion

3.1. Self-assembly of magnetic nanocubes

The self-assembly process of cubic iron-based nanoparticles was analyzed using SEM imaging (Fig. 1(a)). The sample, with a nanoparticle concentration of approximately 30%, exhibits "lego"-type clusters of varying sizes, composed of different numbers of nanocubes. Individual nanoparticles, with sizes ranging from 15 to 20 nm, are shown in the TEM image (Fig. 1(b)). A closer examination of the TEM image reveals that these nanoparticles possess a complex core–shell architecture.

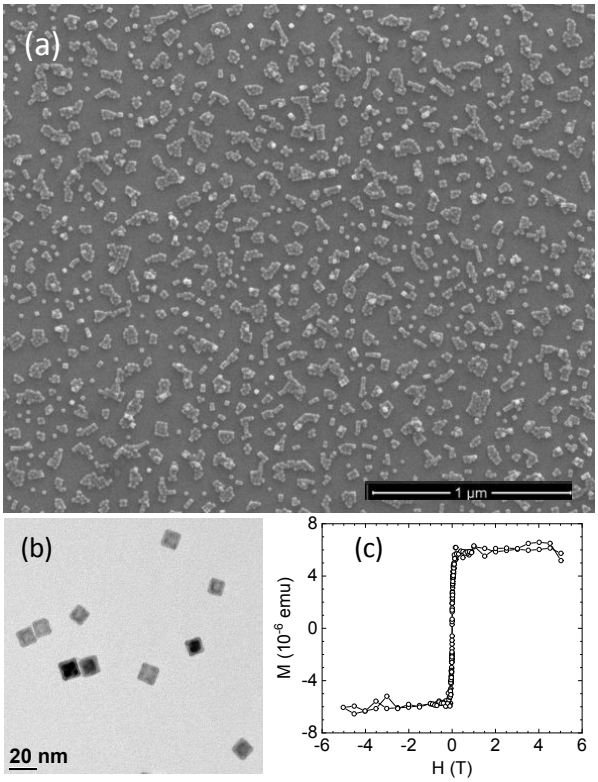

Fig.1 (a) SEM micrograph of self-assembly nanoparticles. (b) TEM image of single Fe/Fe_3O_4 nanoparticle. c) Hysteresis curve at RT.

Specifically, the particles consist of an iron core surrounded by a thin iron oxide shell, formed as a result of oxidation during the cluster-gun preparation process. For nanocubes in the sub-20 nm range, the iron oxide shell thickness is estimated to be about 2.5 nm, corresponding to an iron core size of 15–16 nm.[8] Moreover, this core-shell thickness was in good agreement with the value estimated from electrical characterization of single core/shell iron-based nanoparticles of sub-20 nm size.[8]

The magnetic nature of the iron-based nanocubes is confirmed by hysteresis measurements at RT (Fig. 1(c)). At RT, sub-20 nm complex iron/iron oxide nanoparticles exhibit superparamagnetic behavior (see also Fig.S1 in Supplementary Information), characterized by a closed hysteresis loop.[17] The detailed microstructure, magnetic and electric characterisation of iron core/shell nanoparticles as a function of nanoparticle size under different preparation conditions can be found elsewhere.[8,17]

The small aggregates, assemblies of nanoparticles in direct physical contact, are homogenously distributed all around surface (Fig. 1(a)), forming a contiguous structure with arbitrary cluster geometries. To clarify the self-assembly mechanism, high-resolution field emission SEM was employed. Figure 2 shows representative pictures obtained at varying nanocube concentrations, starting from low surface coverage to completely covered surface with multiple layers of magnetic nanocubes.

At very low nanoparticle concentrations (<10%), the surface exhibits predominantly isolated nanocubes along with small aggregates comprising up to five nanocubes (see insets in Figs. 2(a)–(b)). With increasing concentration (Figs. 2(c)–(d)), larger clusters emerge, although individual nanocubes and doublets remain detectable. As expected, the average cluster size, estimated from[39] $< n >= \sum nG_n / \sum G_n$, increases with increasing nanoparticle concentration from $< n >= 1$ nm for 2% to 6.1 nm for 30 % sample (see Fig. S2 in the Supplementary Information). These assemblies predominantly adopt two-dimensional, close-packed configurations resembling "lego-like" arrangements (Fig. 2(d)), confined largely to a single plane. Occasional nanocubes positioned atop these clusters (highlighted as white dot-like features in Figs. 2(d)–(e)) indicate the onset of three-dimensional stacking. However, this vertical growth is minimal (<4%) compared to the population directly anchored to the silica substrate (Fig. 2(d)).

At higher nanoparticle concentrations, interconnectivity among nanocubes becomes continuous. The organization remains primarily two-dimensional in Fig. 2(e), whereas at the highest concentrations (Fig. 2(f)), pronounced three-dimensional agglomerates are clearly observed. More details can be visualized in Fig.3(a), where the relative number of nanocubes in different configurations is shown for n-particle clusters identified in Fig.2(d). The majority of nanocubes can be found in planar 2D arrangement. The self-assembly of nanocubes in chain are visible for small nanocluster size (still clearly visible in clusters up to 10 nanocubes). On the other side, number of nanocubes stacking atop other nanocubes remains small up to clusters containing 36 nanocubes (see also Table 1). With further increase of nanoparticle concentration, the clear onset

View Article Online
DOI: 10.1039/D6NA00067C

of three-dimensional stacking is rapidly expected, as can be seen in Figs. 2(e) and(f).

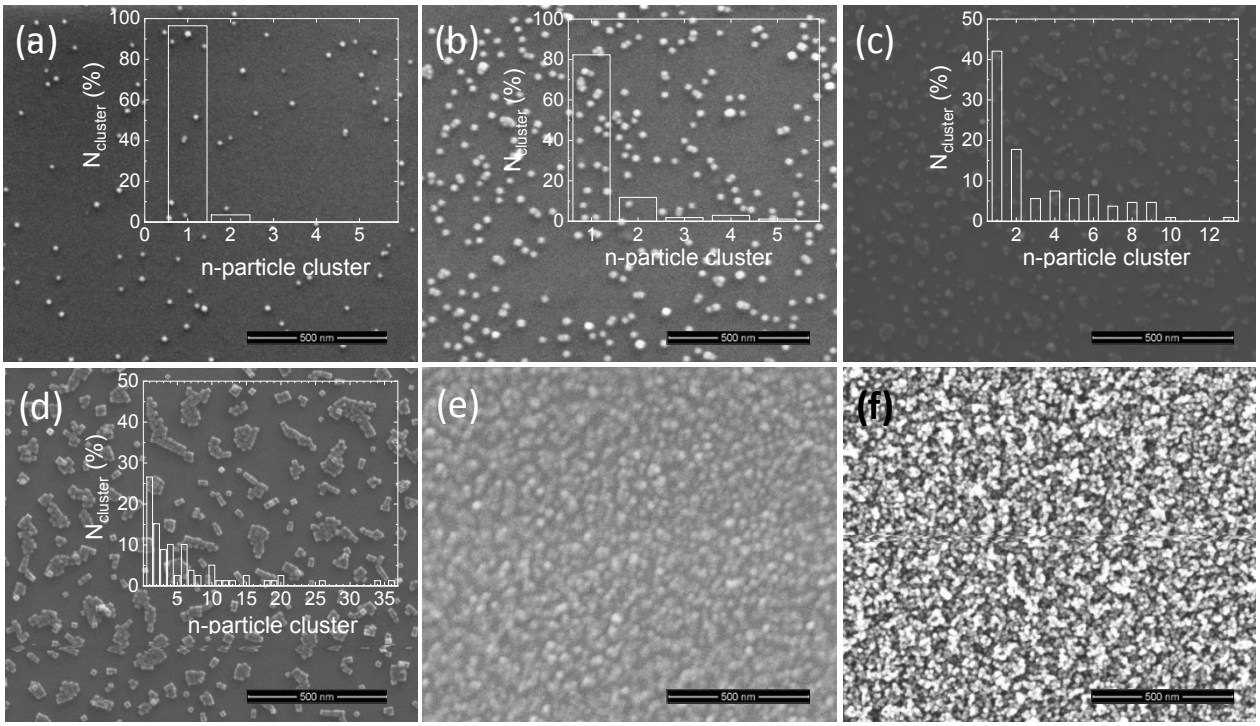

Fig. 2 SEM micrographs of self-assembly nanoparticles for different concentration prepared under similar conditions obtained using different deposition time (a) 2 %, (b) 6 % s, (c) 10 %, (d) 30 % (e) 60 % and (f) completely covered surface. In the inset of (a)-(d), corresponding histogram distribution for nanoparticle concentration below threshold.

At higher concentrations, all clusters are interconnected. As mentioned before, the final cluster configurations provide an insight into the magnetic anisotropy of magnetic building blocks. In the case of magnetic nanocubes with core/shell structure, the direction of the easy magnetic axis is controlled by the core to shell ratio.[13,40] In our case, there are two possible magnetic easy axes, one governed by the magnetite shell lying in the [111] direction and the other governed by the iron core along the [001] direction.[17] To further elucidate nanocube configurations and the potential orientation of their magnetic easy axes, clusters of varying sizes were examined. As shown in Figs. 1(a) and 2(d), for the sample with 30% surface coverage, the majority of nanocubes exhibit face-to-face assembly, corresponding to {100}–{100} facet alignment (see Fig. 3(b) and Table 1). This configuration suggests a preferential orientation of the magnetic easy axis along the cube edges, consistent with the cubic anisotropy of the material.

As cluster size increases, the proportion of perfectly aligned {100}–{100} contacts decreases, and alternative configurations such as edge-to-edge ({100}–{110}) and displaced face-to-face arrangements become more frequent. Nevertheless, face-to-face alignments remain dominant even in large aggregates containing up to 36 nanocubes (see Fig. 3(b) and Table 1 below), indicating that crystallographic matching and minimization of surface energy play a key role in the assembly process.

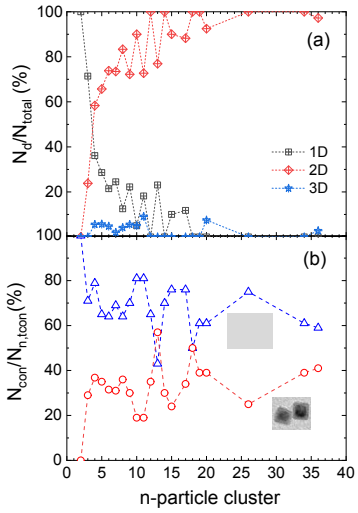

Fig.3 (a) Relative number of nanocubes assembled in different configurations. N_d is a number of nanocubes in face-to-face chain (1D), planar arrangement (2D) and nanocubes attached atop of first nanocube cluster (3D). N_{total} is a total number of cubes identified for a n-particles clusters. (b) Relative number of face-to-face connections vs other configurations in n-particle clusters. N_{con} is number of face-to-face/other configurations and $N_{n,tcon}$ is total number of all connections for n-particles cluster, identified in Fig. 2(d) and pondered by the number of similar configurations. The dot size represents error bar estimated for each n-particle cluster.

View Article Online
DOI: 10.1039/D6NA00676C

Table 1 identifies the number of face-to-face connections and compares them with other possible configurations (edge-to-edge, displaced face-to-face arrangements *etc.*). As previously reported in the literature, in quasi-two-dimensional layers, both [001] and [111] magnetic orientations can promote face-to-face assembly: a collinear head-to-tail arrangement for [001] and a zig-zag pattern for [111] orientation.[15] However, for nanocubes in the sub-20 nm range, the magnetite shell is significantly thinner than the iron core (see Fig. 1(b) and discussion above), indicating that the iron core plays the dominant role in determining magnetic behavior, favoring a [001] magnetic axis orientation.

Moreover, the zig-zag pattern associated with [111] orientation[15] does not adequately explains the magnetic response observed in Fig. 1(c). This interpretation aligns with previous studies showing that core/shell iron nanocubes below 25 nm preferentially adopt a single-domain spin configuration, with magnetization aligned along equivalent [100], [010], and [001] axes of the iron core.[13]

For larger nanocubes (approximately 25 nm in size with an oxide shell around 4 nm thick), previous studies have reported the formation of one-dimensional macroscopic chains. In these cases, atomic and magnetic force measurements identified the [111] magnetic orientation combined with a displaced face-to-face configuration as the most energetically favourable arrangement.[17] In the present study, SEM images (Fig. 1(a) and Fig. 2(d)) reveal both edge-to-edge and displaced face-to-face configurations, indicating that [111] magnetic orientation cannot be completely ruled out for some nanocubes. Nevertheless, the regular "lego"-type clusters observed are more consistent with [001] magnetic alignment and its equivalent [010] and [100] orientations, which likely dominate the assembly process.

It is important to note that, due to the nature of the cluster-gun preparation method, interactions driven by steric effects from residual chemicals and attractive capillary forces—which can promote face-to-face assembly—are completely excluded.[12] In contrast, for clean surfaces, attractive van der Waals interactions are present, scaling with the contact area.[41] These interactions further stabilize the face-to-face configuration and contribute to the formation of the characteristic "lego"-type clusters (see also discussion below) .

Table 1 Some characteristic n-particle clusters in self-assembly of sub-20 nm nanocubes, identified from SEM micrographs. The estimated number of face-to-face versus other configurations is given in 3rd and 4th column respectively, for n–particle clusters (2nd column).

n-cluster configuration	n-cluster	face-to-face	other	n-cluster configuration	n-cluster	face-to-face	other	n-cluster configuration	n-cluster	face-to-face	other
	2	1	0		6	2	4		10	7	5
	3	2	0	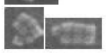	7	7	2		11	10	2
	3	1	2		7	7	4		12	11	6
	4	4	0		7	6	2		13	6	8
	4	3	0	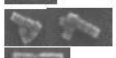	7	5	2		14	14	6
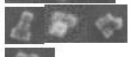	4	2	2		7	4	2		15	10	8
	4	2	1		7	4	4		15	9	9
	4	1	3	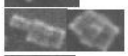	8	8	2		17	20	6
	5	4	0		8	7	3		18	12	12
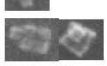	5	4	2		8	6	3		19	16	10
	5	3	1		8	5	3		20	16	10
	5	3	4		8	3	8	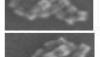	20	12	5
	5	2	3		9	9	0	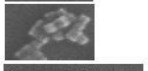	27	30	9
	6	7	0		9	9	3				
	6	6	0		9	6	2		34	26	16
	6	5	0		9	5	4				
	6	4	2		9	4	6		36	20	14
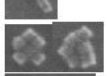	6	3	2		10	17	2				

3.2. AFM manipulation of magnetic "lego" clusters

To further elucidate the nanocube behaviour, we now focus on investigating the response of these "lego"-structures to mechanical shear forces. The nanocubes already form different self-assembled clusters governed by their magnetic interactions before AFM manipulation experiments. To this end, we employ AFM manipulation in contact mode, which enables the application of shear forces and tip-induced displacement of nanocubes, along with simultaneous measurement of lateral forces between the AFM tip and the nanocubes.

Elastic response of magnetic "lego" clusters. In the first AFM experiment, single layer of magnetic nanocubes was manipulated by raster scanning in contact mode across eight horizontal stripes of increasing length (from 0.5 μm to 4 μm) and constant width (120 nm), as depicted in Fig. 4(a). The applied normal load during manipulation was 90 nN. The topography of the stripes recorded during the manipulation process, is shown in Fig. 4(b). The dark contrast observed within the stripes indicates that the nanocubes were removed during manipulation. This is further confirmed by the height profiles measured along the stripes, displayed in Fig. 4(c). As seen, the profiles are nearly flat, with superimposed height fluctuations of approximately one nanometer, which is far below the nanocube size. In addition, the observed height peaks are small, only a few nanometers high, and they cannot be attributed to the nanocubes remained within the stripes.

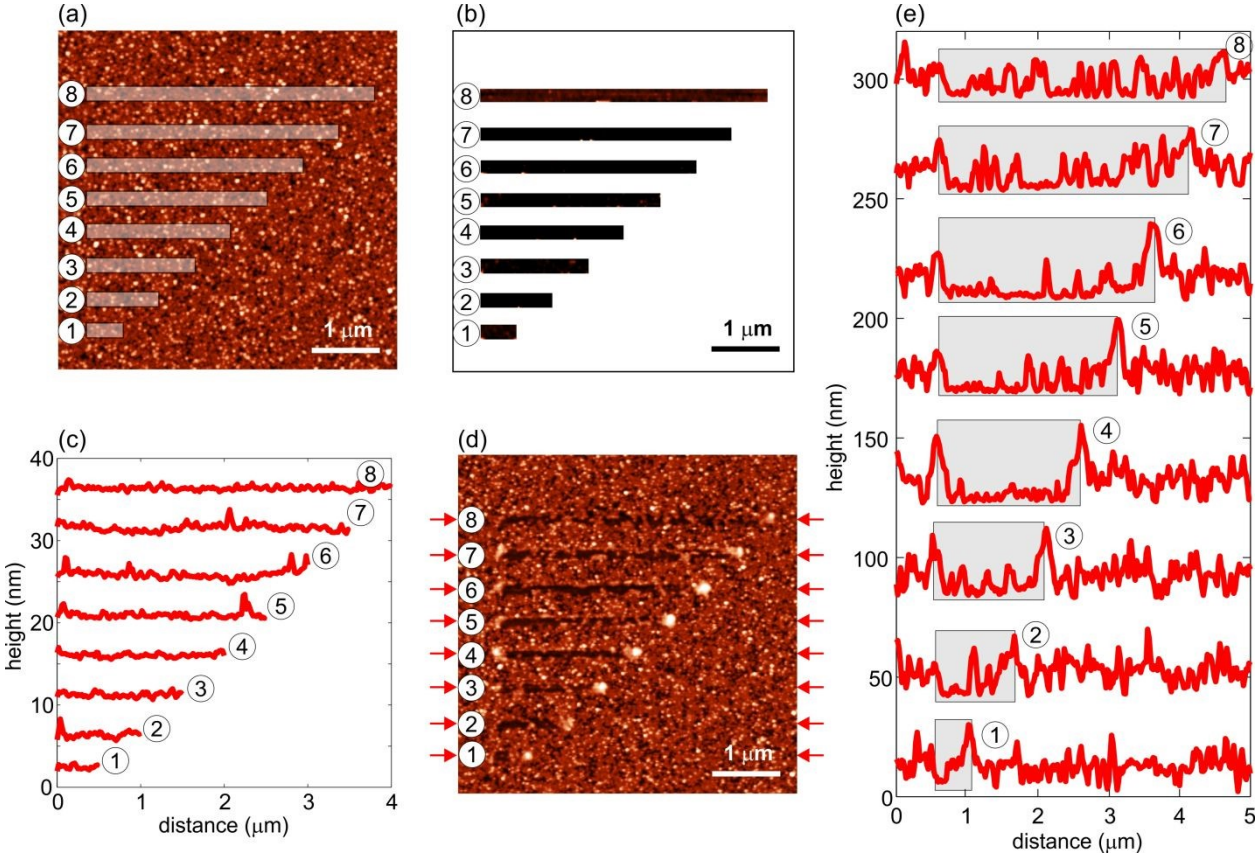

Fig.4 (a) Initial topography of single layer containing magnetic nanoparticles (z-scale is 0-30 nm). The eight grey stripes (1-8) indicate the regions where AFM manipulations were performed. (b) Topographies of the eight stripes recorded during the manipulations in contact mode (z-scale is 0-5 nm). The stripes appear nearly completely dark, suggesting flat regions resulting from the removal of nanocubes along the AFM tip path during manipulation. (c) Height profiles measured along the eight stripes shown in part (b). (d) Topography of the magnetic nanoparticle layer recorded in tapping mode after the AFM manipulations (z-scale is 0-30 nm). (e) Height profiles measured along the arrows indicated in part (d). The shaded rectangles in part (e) denote the regions (stripes) where the AFM manipulations were carried out.

The topographic image of the entire region containing the eight stripes, recorded in tapping mode after manipulation, is displayed in Fig. 4(d). Narrow, dark horizontal regions indicate trenches formed within the layer of magnetic nanocubes. These trenches correspond to the horizontal stripes where manipulation was performed. However, in contrast to Fig. 4(b), the trenches in Fig. 4(d) display irregular edges and varying widths, while they appear completely closed by nanocubes at certain locations. This is also illustrated by the corresponding height profiles in Fig. 4(e), manipulated along the horizontal stripes. The regions previously scanned in contact mode are highlighted by grey rectangles. Except for the fourth stripe, all

others exhibit pronounced height peaks of around 15 nm, corresponding to the nanocubes that remained after AFM manipulation. These results suggest that after the AFM tip passes through the layer of magnetic nanocubes, they tend to realign and reorganize into patterns influenced by their mutual magnetic interactions. As a result, many of the nanocubes returned into the regions of the horizontal stripes from which they were previously removed by the AFM tip.

This example demonstrates that the layer of magnetic nanocubes exhibits elastic-like behavior. As shown in Ref.[42], a chain of magnetic particles can behave analogously to an elastic rod. When a mechanical load is applied to the straight chain consisting of spherical particles with all magnetic dipole moments aligned along the chain axis, the chain bends, causing misalignment of the dipoles. This misalignment induces magnetic torques that resist the imposed bending. As demonstrated before[42], this phenomenon can be quantitatively described in terms of an effective bending stiffness (also known as flexular rigidity). Therefore, the magnetic interactions between neighboring particles provide a restoring torque that tends to return the chain to its original configuration once the external load is removed.

A similar behavior is observed in the present case. Magnetic nanocubes initially organize into planar layers. When shear force is applied by the AFM tip, the system experiences a localized perturbation. Nanocubes along the tip's path may be completely removed from the layer, while others are only slightly displaced from their equilibrium positions. In the latter case, the interaction with neighboring nanocubes act as a restoring force. After the AFM tip passes, this restoring force drives the displaced nanocubes toward a new equilibrium configuration. As a result, these nanocubes tend to return to the horizontal stripes previously scanned by the AFM tip. These observations indicate that densely packed layers of magnetic nanocubes exhibit an elastic-like response.

Shape-persistent magnetic "lego" clusters. In the second AFM experiment, a cluster of magnetic nanoparticles, shown in Fig. 5(a), was pushed multiple times in both the horizontal and vertical directions (marked by the arrows in Figs. 5(a)–(e)) using the AFM tip in contact mode. The applied normal load was 20 nN. Figures 5(b)–(f) display the resulting topographies of the cluster, recorded in tapping mode after each manipulation step. Unexpectedly, the cluster remained quite stable. Only after the fifth manipulation step, three small fragments (marked by the arrows in Fig. 5(f)) were detached from the main cluster. This is an unusual behavior, since clusters of nanoparticles typically disintegrate easily under applied mechanical load.

Shape-persistent clusters made from gold nanoparticles have only been achieved when ligands were carefully selected to facilitate interparticle interactions through hydrogen bonding.[43] The shape-persistency of these gold clusters was confirmed via AFM manipulation experiments, analogous to those conducted in our study. However, a crucial difference between the two cases is that the magnetic nanocubes in our study are free of any ligands, as they are fabricated by a gas aggregation cluster source. Therefore, such nanoparticles enable the study of intrinsic nanocube interactions in the absence of ligand-induced steric interactions, unlike traditional wet-chemistry methods. Finally, the observed mechanical stability of investigated clusters suggests the presence of strong interparticle interactions among the magnetic nanocubes, making them an excellent platform for the fabrication of shape-stable magnetic clusters.

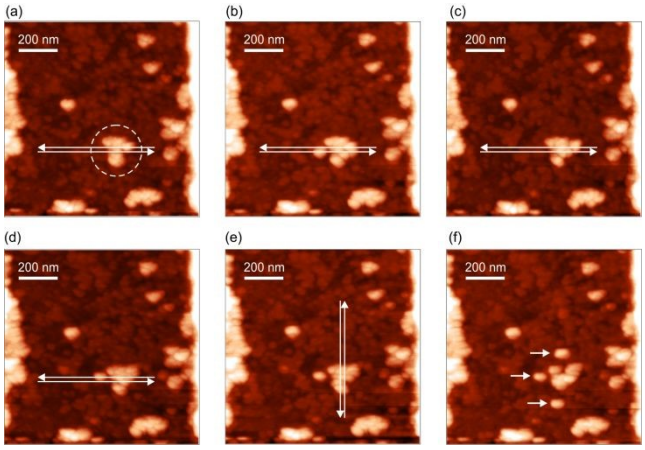

Fig.5 (a) Initial topographic image of the cluster of magnetic nanoparticles, outlined by the dashed line (z-scale is 0-23 nm). (b)–(f) Topographic images of the cluster after AFM manipulations in contact mode along the paths indicated by the arrows (z-scale is 0-23 nm). Each image (b)-(f) was recorded in tapping mode and corresponds to the result of the manipulation along the path shown in the preceding image (a)-(e), respectively. The arrows in (f) indicate three small fragments that detached from the main cluster following all manipulation steps.

Shear-induced alignment of magnetic "lego" clusters. The results of AFM manipulation of a monolayer of magnetic nanoparticles across square regions are presented in Figs. 6(a1)–(a4). Each image represents the topography recorded in contact mode during the manipulation process. The manipulation was carried out using raster scanning, starting from the bottom-left corner of the selected area. The scanned area was divided into ten horizontal stripes, as indicated by the arrows in Fig. 6(a1). During scanning, the normal load was progressively increased from the bottom to the top, while remaining constant within each stripe. The applied normal load ranged as follows: 0.60–1.90 nN in the first step (Fig. 6(a1)), 2.10–3.40 nN in the second step (Fig. 6(a2)), 3.50–4.90 nN in the third step (Fig. 6(a3)), and 5.00–6.30 nN in the fourth step (Fig. 6(a4)).

At first glance, Figs. 6(a1)–(a4) reveal that magnetic nanoparticles (appearing as bright regions) were progressively removed from the silica substrate (shown as dark regions) as the normal load increased. Consequently, the exposed substrate area is significantly larger after the fourth

manipulation step (Fig. 6(a4)) compared to the first step (Fig. 6(a1)). More notably, the mechanical interaction with the AFM tip induces a reorganization of the magnetic nanoparticles, causing them to organize into short chain-like structures with near-linear alignment. The chain-like structures are even better resolved in lateral force images presented in Figs. 6(b1)–(b4). Although AFM images do not provide the same spatial resolution as SEM images, the short chains observed in the AFM images seems to consist of several nanocubes, resembling to the chains presented in Table 1.

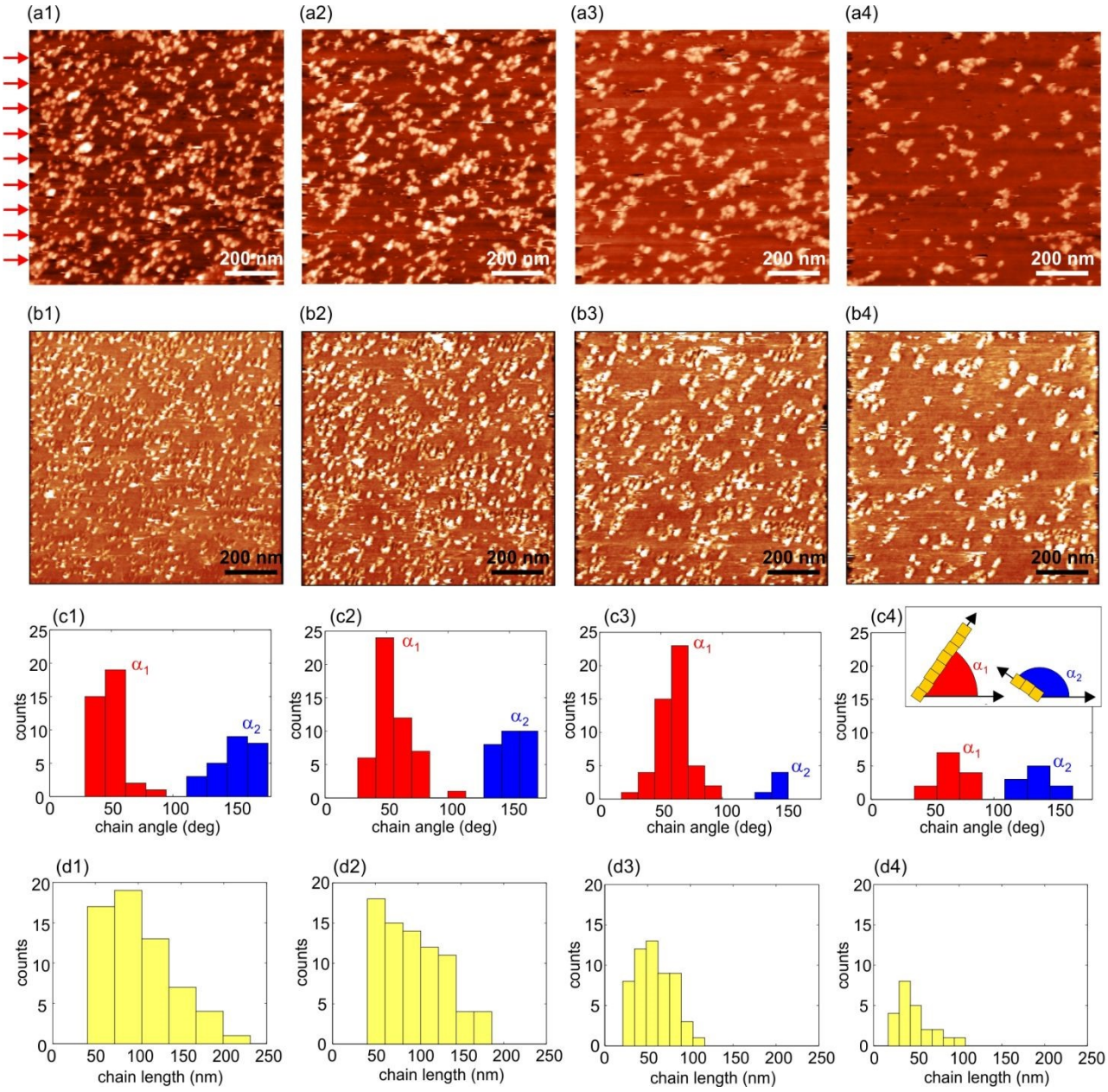

Fig.6 (a1)-(a4) Topography of magnetic nanocubes recorded in contact mode simultaneously during AFM manipulations for the manipulation steps from 1 to 4, respectively (z-scale is 0-25 nm in parts (a1) and (a2), and 0-35 nm in parts (a3) and (a4)). In each image, the normal force was incrementally increased from the bottom to the top (with the load held constant within each individual stripe which marked by the arrows in part (a1)). (b1-b4) Lateral force maps recorded simultaneously during each manipulation step (z-scale are the following: (b1) 0-4.90 nN, (b2) 0-5.80 nN, (b3) 0-6.60 nN, and (b4) 0-7.40 nN). (c1)-(c4) Histograms of chain angles with respect to the fast-scan axis (x-axis) in degrees calculated from corresponding topographic images in parts (a1)-(a4). (d1)-(d4) Histograms of chain lengths in nanometers calculated from corresponding topographic images in parts (a1)-(a4).

View Article Online
DOI: 10.1039/D6NA00676G

Visual inspection of Figs. 6(a1)–(a4) and 6(b1)–(b4) reveals that these chains are predominantly oriented toward the top-right corner of the images. At the same time, these images also show less frequent and shorter chains which are oriented toward top-left corner. The chain angle is defined as the angle between a chain and the fast-scan axis (x-axis) as illustrated in the inset of Fig. 6(c4). Corresponding angle distributions after each manipulation step are presented in Figs. 6(c1)–(c4). In each case, two preferential chain angles are observed: one centered around $\alpha_1 \approx 50°–60°$, corresponding to longer and more frequent chains oriented toward the top-right corner, and another centered around $\alpha_2 \approx 140°–150°$, associated with shorter and less frequent chains oriented toward the top-left corner. The fact that these chains are linear and oriented at a well-defined angle with respect to the reference x-axis implies face-to-face orientations between the constituent nanocubes. The two preferential chain orientations α_1 and α_2 differ by approximately 90°, indicating that the chains are nearly orthogonal to each other as schematically depicted in the inset of Fig. 6(c4). Many of these orthogonal chains intersect with one other, as shown in Figs. 6(a1)-(a4) and 6(b1)-(b4). The mutual orthogonality of the intersecting chains further supports the presence of face-to-face connections between nanocubes at the intersection points.

AFM manipulation of nanoparticles during raster scanning, whether in contact or tapping mode, is well known to cause their displacement along the effective direction of AFM tip movement.[24,25] In the present case, scanning began at the bottom-left corner. During the forward (trace) scan from left to right, the AFM tip effectively moved toward the top-right corner, promoting the reorganization of nanocubes into chains aligned along the α_1 direction. Conversely, the backward (retrace) scan from right to left contributed to partial reorganization of nanocubes into chains oriented along the α_2 direction. Therefore, the observed rearrangement of nanocubes into chains is primarily induced by shear forces due to the AFM tip motion. Similar rearrangements and nanoparticle organizations are expected for both magnetic and non-magnetic nanoparticles. However, the observed chain geometry is most consistently explained by magnetic interactions between the nanocubes. In particular, the linear alignment and the occurrence of junctions at approximately 90° are indicative of a preferred face-to-face orientation mediated by magnetic dipolar interactions, which is not typically observed for non-magnetic nanoparticle assemblies under similar shear conditions.

Histograms of chain lengths for each manipulation step are shown in Figs. 6(d1)–(d4). The average chain length decreases from nearly 100 nm to less than 50 nm, while the maximum chain length decreases from over 200 nm to approximately 100 nm after the fourth manipulation step. Simultaneously, the number of observed chains (as indicated by the count data) drops significantly after the fourth manipulation step. These results indicate that mechanical forces applied by the AFM tip fragment longer chains into smaller ones. With a further increase in normal load during AFM manipulation, the chains almost disappear (see Fig. S3 of Supplementary Information).

Interaction between nanocubes. In order to study nanocubes interaction we focus on a sample composed of multiple layers of magnetic nanocubes, corresponding to a higher concentration (see Fig. 2(e)). The initial AFM morphology of the sample is shown in Fig. 7(a). AFM manipulation was performed by raster scanning a central square region of $1 \times 1\ \mu m^2$. The normal force was held constant within the entire region during each of the four manipulation steps (F_N was 19 nN, 30.60 nN, 55.80 nN and 30.60 nN in the first, second, third, and fourth manipulation steps, respectively). The surface morphology recorded in tapping mode after each manipulation step is shown in Figs. 7(b)–(e). The morphology after the final (fourth) manipulation step is shown again in Fig. 7(f), with the color scale emphasizing grainy structure of the bottom layer of magnetic particles that became exposed after the top layer was removed by the AFM tip. The height profile in Fig. 7(f) further illustrates the central region (between 0.5 μm and 1.5 μm) from which magnetic particles were removed. Step heights of approximately 15 nm are observed at the boundaries of this region, around 0.5 μm and 1.5 μm, marking the transition from the exposed bottom layer to the surrounding top layer of particles.

In the previous sample analyzed in Fig. 6, a single layer of magnetic nanocubes was deposited on a non-magnetic substrate such as silica. In contrast, the current sample consists of a top layer of magnetic nanocubes positioned on an underlying magnetic layer of similar nanoparticles, introducing an additional magnetic interaction within the system. As a result, the nanocubes in the upper layer are more strongly bound to the surface, which significantly restricts their mobility. This effect is first evidenced by the higher normal forces required to initiate nanoparticle displacement during AFM manipulation. In the earlier case, the applied normal forces ranged from 0.60 to 15.60 nN, whereas in the present case, they increased substantially, varying between 19 and 55.80 nN.

The topographic image recorded after the first manipulation step (Fig. 7(b)) displays irregularly shaped holes, visible as dark contrast areas. Magnetic nanocubes in the top layer were removed from these regions. However, no accumulation of displaced nanocubes is observed either within the manipulated square region or along its edges. This suggests that the nanocubes removed during the first manipulation step were only marginally displaced from their original positions. Rather than undergoing significant lateral movement, the AFM manipulation primarily results in a spatial reorganization of the nanocubes into various clusters and into elongated and wide chains. Typical examples of such structures are highlighted in Fig. 7(b). Self-assembly of magnetic nanoparticles into similar structures has been reported for both clusters[21,15,5,44,45] and chains[20,,44,45].

View Article Online
DOI: 10.1039/D6NA00636

The fact that the nanocubes were merely reorganized rather than displaced provides additional confirmation of the significant interparticle interactions among the magnetic nanocubes that prevent their separation. However, at higher normal loads, we first observe the fragmentation of magnetic clusters and then pronounced accumulation of nanocubes along the right and left edges of the manipulated square region as shown in Figs. 7(c)-(e). In these cases, the increased mechanical forces exerted by the AFM tip are sufficient to overcome the mutual interactions between nanocubes, facilitating their displacement over longer distances. Still, even in these cases, smaller magnetic clusters can be observed within the scanned area after each manipulation step, as shown in Figs. 7(c)– (e).

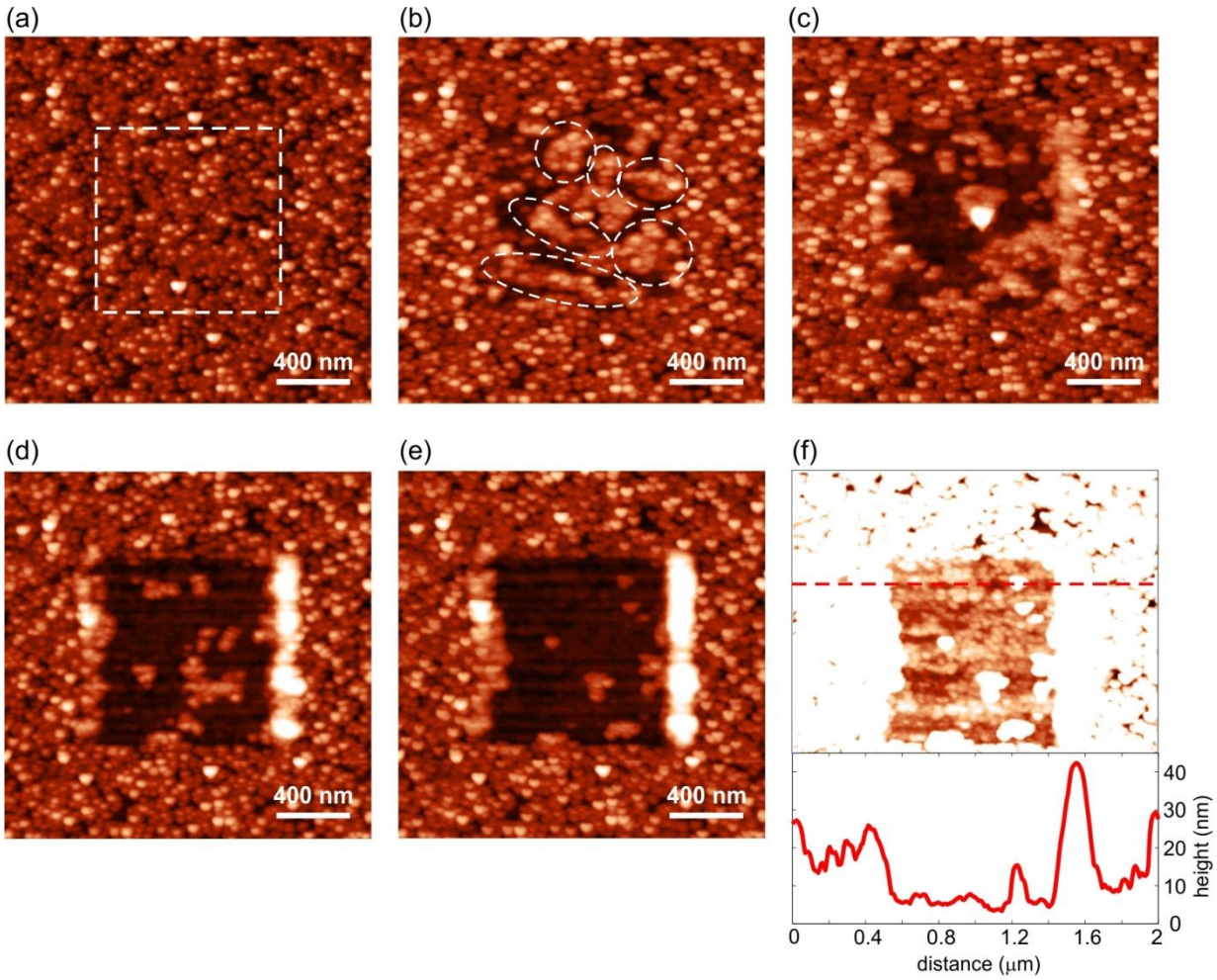

Fig. 7 (a) Initial topography of the sample with double layer of magnetic nanoparticles recorded in tapping mode (z-scale is 0-30 nm) with square region for AFM manipulation marked by the dashed line. (b)-(e) Sample topography measured in tapping mode after four sequential AFM manipulations within the inner square 1×1 μm2 region (z-scale is 0-30 nm). The AFM manipulations were conducted by raster scan in contact mode under increasing normal load F_N. (f) The topography as in part (e) but with the color scale (z-scale is 0-10 nm) emphasizing the bottom layer of magnetic nanoparticles revealed after the AFM manipulation. The bottom part of part (f) displays the height profile along the dashed line.

View Article Online
DOI: 10.1039/D6NA00056C

The topographic image acquired in contact mode during the first manipulation step is shown in Fig. 8(a). As seen, the image displays abrupt "cuts" where particle images are suddenly interrupted. This behavior is characteristic of AFM manipulation experiments involving particle displacement, as schematically presented in Fig. 8(b). During raster scanning in contact mode, the AFM tip traces the nanoparticle (as indicated by blue arrows) as long as the applied normal load remains below the threshold force required to initiate movement. Once this threshold is exceeded, the AFM tip displaces the nanoparticle (along the path indicated by the red arrow) from its initial position 1 to a new location with position 2. The resulting image of the nanoparticle then consists of two distinct segments. The first segment, labelled as part 1, corresponds to the nanoparticle at its initial position and it was recorded from the top of the scan down to the point where movement occurred. At that moment, the image is abruptly interrupted. The second segment labelled as part 2, begins at the nanoparticle's final position 2 and continues from that point to the end of the scan. Figure 8(c) provides an enlarged topographic view of the region highlighted in Fig. 8(a), illustrating an experimental observation of a single nanoparticle displacement and its impact on the AFM image, as conceptually depicted in Fig. 8(b). In Fig. 8(c), the same nanoparticle appears split into two distinct segments due to its movement during scanning. Since the scan began from the top, segment 1 corresponds to the nanoparticle's initial position, while segment 2 represents the lower portion of the nanoparticle imaged after its displacement to the right, at its final position. This image splitting caused by nanoparticle motion is further confirmed by the height profiles shown in Fig. 8(c). The two profiles, acquired from each part of the nanoparticle image, reveal a lateral displacement of approximately 100 nm.

In order to study the interaction between nanocubes, we recorded lateral force signals during manipulation experiments. Generally, the lateral force signal corresponds to the torsional deflection of the AFM cantilever during scanning in contact mode. This torsion typically arises from the friction between the AFM tip and the substrate surface. A significant increase in cantilever torsion is observed when nanoparticles are displaced by the AFM tip, due to additional friction between the nanoparticles and the substrate.[26,27,46] However, in the present case, it is also necessary to consider the interactions between magnetic nanoparticles. Specifically, to move a nanoparticle sideways, the AFM tip must supply enough energy to overcome interactions with neighbouring particles.

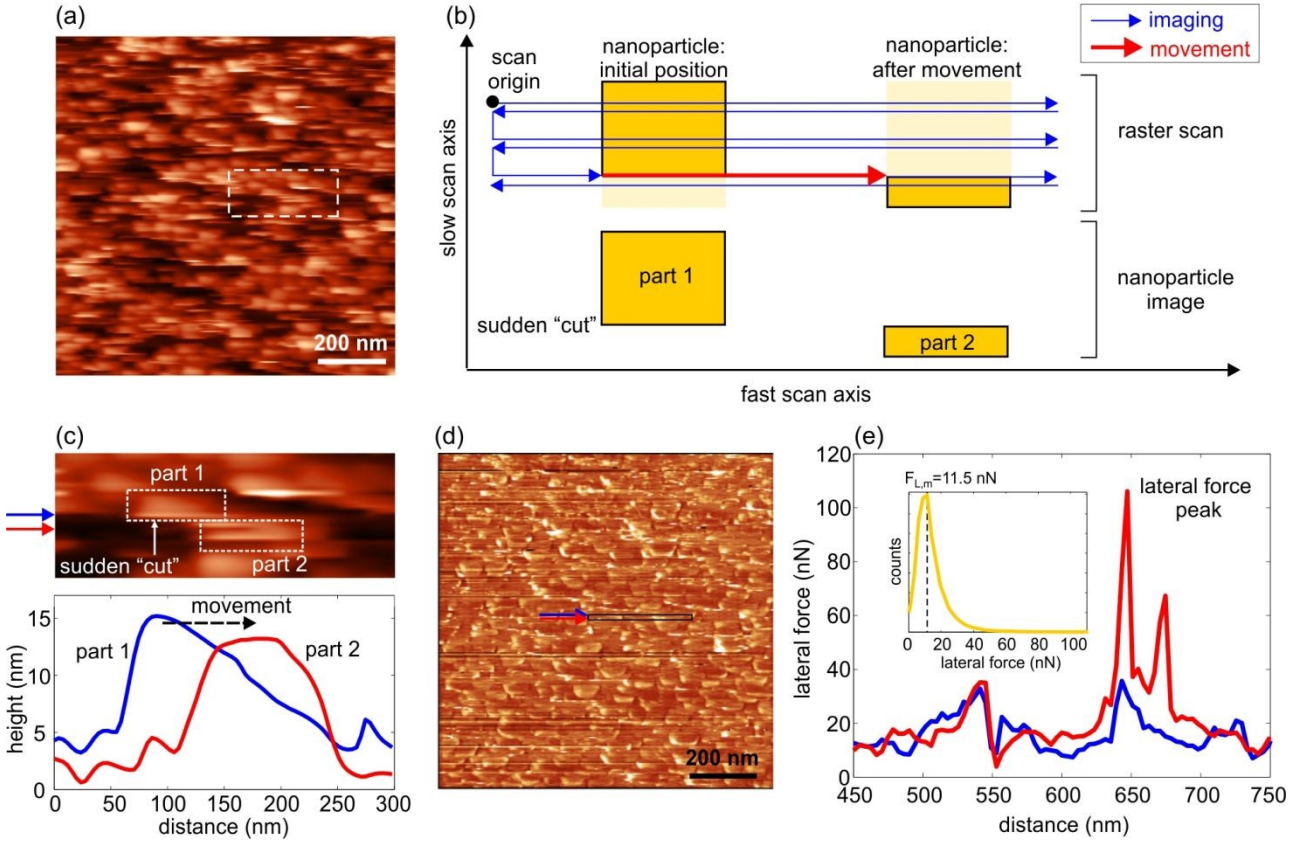

Fig. 8 (a) Topography (z-scale is 0-25 nm) recorded in contact mode during the first manipulation step from Fig. 7(b). (b) Schematic illustration of nanoparticle imaging and movement. (c) Top part: topography (z-scale is 0-20 nm) of the region in part (a) encircled by the dashed line. Bottom part: height profiles before (marked by the blue arrow) and after (marked by the red arrow) the sudden "cut" in the topographic image. (d) Lateral force (z-scale is 0-56 nN) during the first manipulation step. (e) Lateral force profile measured along two arrows within marked rectangle in part (d).

View Article Online DOI: 10.1039/D6NA00067C

The lateral force map recorded in contact mode during the first manipulation step is shown in Fig. 8(d). Similar to the previous case (the lateral force maps in Figs. 6(b1)-(b4)), this map reveals a network of bright points corresponding to lateral force peaks, which indicate pronounced torsional deflection of the AFM cantilever. Two lateral force profiles shown in Fig. 8(e) were extracted along the arrows marked within the encircled region in Fig. 8(d), which corresponds to the topographic image in Fig. 8(c). The lower profile represents the sudden "cut" observed during the manipulation experiment, where the nanocube was displaced, while the upper profile is provided for comparison. As seen, the lower profile exhibits two sharp peaks, which correspond to the displacement of the nanocube shown in Fig. 8(c). The strong spatial confinement of these lateral force peaks indicates that the motion of magnetic nanocubes induced by the AFM tip is significantly constrained by their mutual interactions. In contrast to the AFM manipulation of conventional nanoparticles, which is typically characterized by a prolonged increase in lateral force, the present case exhibits increased forces only within narrow spatial regions. This suggests that the displacement of magnetic nanocubes involves short, localized events rather than continuous sliding.

The inset of Fig. 8(e) shows the histogram of the lateral force map presented in Fig. 8(d). The histogram exhibits single and well-pronounced peak (histogram mode) at $F_{L,m}$=11.5 nN. This lateral force corresponds to the friction force measured on a layer of magnetic nanocubes under a normal load of F_N= 19 nN. Namely, according to classical Amontons' law of friction $\boldsymbol{F_{fr} = \mu_{fr} F_N}$, where F_{fr} and μ_{fr} are the friction force and friction coefficient, respectively, while F_{fr} is always smaller than F_N because μ_{FR} is less than one ($\boldsymbol{\mu_{fr} < 1}$). Therefore, the measured F_L and the applied F_N are consistent with Amontons' law. However, both the histogram and lateral force profiles in Fig. 8(e) shows a significant number of points with lateral forces exceeding the applied normal load. Namely, the lateral force peak values measured during AFM manipulation of nanocubes, as shown in Figs. 6(b1)-(b4) and 8(e), are in the order of several nanonewtns to several tens of nanonewtons. These lateral force peaks arise due to the lateral movement of nanocubes and clearly do not correspond solely to friction. Instead, the lateral movement of a nanocube requires overcoming all interactions with adjacent nanocubes. Therefore, the observed lateral force peaks must be sufficient to surpass the sum of all interparticle interactions.

3.3 Discussion

To elucidate the interactions between magnetic nanocubes, we consider three classes of interparticle forces: magnetic, van der Waals and capillary forces. To estimate the magnetic force between investigated nanocubes, we consider the simplest case of two nanocubes, each possessing axially aligned dipoles with identical magnetic moments μ. The magnetic force between the two nanocubes is given by $\boldsymbol{F_m = \frac{3\mu_0}{2\pi}\mu^2/r^4}$ where μ_0 is the vacuum permeability and r is the center-to-center distance between the nanocubes.[47] For 15 nm nanocubes in contact, this distance is r=15 nm. The magnetic moment is calculated as $\boldsymbol{\mu = MV}$, where V is the volume of the nanocube and M is its magnetization. The considered nanocubes consist of an Fe core and an Fe_3O_4 shell. The bulk magnetizations for Fe and Fe_3O_4 are 1346 kA/m and 476 kA/m, respectively.[48] Although magnetization typically decreases in nanoparticles and thin films[47], we use these bulk values for an initial estimation. To estimate the magnetization of the core-shell nanocube, one would need to know the volume fractions of each component and then to weight their magnetizations accordingly. For simplicity, we assume an average magnetization of 1000 kA/m. Using this approximation, the resulting magnetic force between two touching 15 nm nanocubes is approximately 130 pN. An increase in the nanocube separation of 1 nm, 2 nm and 3 nm reduces the magnetic force to 104 pN, 82 pN and 65 pN, respectively, corresponding to a gradual decrease of approximately 50% at the 3 nm separation.

Van der Waals force between two nanocubes with a face-to-face connection is $\boldsymbol{F_{vdW} = A_H a^2/(6\pi D^3)}$, where A_H is the Hamaker constant, a is the nanocube side length, and D is the separation between the two nanocubes.[40] The nanocubes have core–shell structures, but since the van der Waals force decays very rapidly with a distance, it is reasonable to assume that it is dominantly determined by the Hamaker constant of the iron-oxide shell, which is approximately $A_H \approx 10^{-19}$J for Fe_3O_4.[41] We therefore assume that F_{vdW} originating from the iron cores is screened by the oxide shells. Still, this does not introduce a significant difference in the estimated force, since the Hamaker constant for metals is only slightly larger. In the case of touching nanocubes with a=15 nm, distance between them is taken as D=0.3 nm (the gap between nanocubes is determined by an interatomic distance since touching nanocubes do not imply D=0 nm). Finally, the estimated van der Waals force between touching nanocubes and in a face-to-face configuration is around 40 nN. This value represents an estimate of the maximal F_{vdW}. For edge-to-edge connections and more separated nanocubes, the van der Waals force would be lower. Upon increasing the separation between the nanocubes by 1 nm, 2 nm, and 3 nm, the van der Waals force decreases to 1.2 nN, 150 pN, and 44 pN respectively. Thus, even a modest increase in separation to 2 nm reduces the van der Waals force by more than two orders of magnitude, making it comparable in magnitude to the magnetic force. With a further increase in separation, the magnetic force becomes dominant.

Furthermore, since the measurements were performed under ambient conditions with a relative humidity of approximately 50%, capillary forces cannot be neglected. These attractive forces arise from the formation of a liquid meniscus between nanocubes (also between nanocubes and the substrate). In order to estimate capillary interaction between magnetic

View Article Online
DOI: 10.1039/D5NA00667J

nanocubes, we consider the capillary force between two identical spherical particles (the spherical particle model was used to estimate the order of magnitude of the capillary force as there is no simple analytical expression for the case of two cubes):

$\boldsymbol{F_{cap}(D) = 2\pi\gamma_W R_{eff}(2\cos\Theta - D/r_c)}$, where γ_W is water surface tension (0.072 N/m at room temperature), $R_{eff}=R/2$ is the effective radius and R is the sphere radius, $\boldsymbol{\Theta}$ is contact angle, D is a distance between the spheres, and r_c is the liquid curvature.[49] As iron-oxide is hydrophilic, it is reasonable to assume a small contact angle leading to $\boldsymbol{\cos\Theta \approx 1}$ (contact angle of water measured on Fe_3O_4 films is 17°,[50] while generally, it is further decreased in the case of nanoparticles). Next, we assume that the sphere diameter ($2R$) is equal to the side length of magnetic nanocubes (15 nm) leading to R_{eff}=3.75 nm. The liquid curvature was calculated from Kelvin equation as $\boldsymbol{r_c = 2\gamma_W V_m/(RT|\ln(RH)|)}$, where V_m=18·10^{-6} m^3/mol is the molar volume of the water, R=8.31 J/(mol K) is gas constant, T=298 K is a room temperature, and RH=0.5 is relative humidity (expressed in the range 0-1). For particles in contact, the capillary force is thus F_{cap}≈3 nN. With increasing nanocube separation, the force decreases linearly to 2.1 nN and 0.9 nN at distances of 1 nm and 2 nm, respectively. At a separation of about 3 nm, the capillary force vanishes, indicating the rupture of the liquid meniscus between the nanocubes.

Finally, based on the analysis above of the three most relevant interactions between magnetic nanocubes, at separations larger than 2–3 nm, the magnetic dipolar interaction is practically the only relevant force. The TEM image in Fig. 1(b) indicates a similar gap between two adjacent nanocubes. Accordingly, the magnetic force appears to govern the assembly of the nanocubes. Moreover, when a shear force is applied to such nanocubes, the magnetic force predominantly determines their elastic-like response or alignment, as observed in Figs. 4 and 6, respectively. In contrast, at very small separations, where the nanocubes are essentially in contact, the capillary and van der Waals forces exceed the magnetic force by approximately one and two orders of magnitude, respectively. At the same time, the estimated magnitudes of these two forces are consistent with the lateral force peak values measured during AFM manipulation of nanocubes. Therefore, it is reasonable to conclude that these two attractive forces between touching nanocubes are primarily responsible for maintaining their shape and overall mechanical stability.

The surface roughness of the silicon substrates used in this work is below 0.5 nm, which is more than 30 times smaller than the nanocube size (~15 nm). Therefore, substrate roughness is expected to have a negligible effect on nanocube assembly and AFM-induced lateral motion, as it does not significantly contribute to mechanical interlocking or alter particle–substrate interactions at this length scale. In contrast, for a double layer of nanocubes, when a nanocube in the upper layer moves, the lower layer effectively acts as the substrate. Unlike a flat silica surface, this substrate exhibits pronounced height variations due to the gaps between adjacent nanocubes. The increased surface roughness can promote mechanical interlocking between nanocubes, thereby enhancing the interaction forces.

Conclusions

In this work, we have experimentally investigated the self-assembly and AFM manipulation of ligand-free Fe/Fe_3O_4 nanocubes synthesized via a gas aggregation cluster source, thereby eliminating steric and capillary contributions typically associated with wet-chemistry. This methodology enables isolation of magnetic dipolar and surface forces as the primary drivers of cluster formation. Our results demonstrate that sub-20 nm nanocubes spontaneously organize into close-packed, two-dimensional clusters characterized by dominant {100}–{100} face-to-face contacts. Structural analysis and magnetic characterization indicate a preferential [001] magnetic easy axis, consistent with Fe-core-dominated anisotropy arising from the presence of a thin magnetite shell.

AFM manipulation experiments reveal that nanocube monolayers exhibit localized, reversible displacements and realignment into previously scanned regions, indicative of a restoring force mediated by dipolar interactions. Furthermore, compact nanocube clusters maintain structural integrity under repeated orthogonal perturbations, with only minor fragmentation occurring at high loads, underscoring strong interparticle magnetic coupling and mechanical stability even in the absence of organic ligands. Under conditions of raster scanning with progressively increasing normal load, nanocubes reorganize into short chains (≈50–200 nm) exhibiting two preferential orientations (α_1 ≈ 50°–60°, α_2 ≈ 140°–150°), reflecting the effective direction of tip-induced shear.

The mobility of nanocubes is strongly layer-dependent. When nanocube multilayers are formed, a much higher normal loads are needed to initiate motion than in monolayers, due to the additional magnetic coupling to the underlying nanocube layer. Lateral force mapping reveals spatially localized peaks corresponding to discrete displacement events rather than continuous sliding, contrasting with the behavior of non-magnetic nanoparticles. Comparison between estimated dipolar forces and measured lateral forces suggests that magnetic coupling operates synergistically with van der Waals attraction, frictional dissipation, mechanical interlocking on rough particle carpets, and capillary forces under ambient humidity. These findings establish magnetic nanocubes as robust and reconfigurable building blocks for shear-assisted assembly of mechanically stable magnetic architectures. The ability to control orientation, induce chain formation, and achieve structural recovery through tip-mediated shear provides a promising route toward programmable patterning of two- and three-dimensional magnetic networks. Overall, the findings demonstrate that these iron-based nanocubes behave as shape-persistent magnetic building blocks whose assembly and reconfiguration can be directed by shear, with their

View Article Online
DOI: 10.1039/D6NA00067C

mechanical response governed primarily by dipolar coupling in clean, ligand-free conditions.

Author contributions

BV, ZK: Writing – original draft, Visualization, Methodology, Investigation, Analysis, Discussion. LlB, NM, BM, AP: Writing, Analysis, Discussion.

Conflicts of interest

There are no conflicts to declare.

Data availability

Data for this article, including figures and analysis are available on CSIC institutional repository DIGITAL.CSIC (https://digital.csic.es).

Acknowledgements

BV and ZK acknowledge funding provided by the Institute of Physics Belgrade, through the grant of the Ministry of Education, Science, and Technological Development of the Republic of Serbia. This work has received funding from the State Investigation Agency, through the Severo Ochoa Programme for Centres of Excellence in R&D (CEX2023−001263-S) and "ETMOS" (PID2024-155387OB-I00). We acknowledge the contribution from ICMAB-CSIC's Scientific & Technological Services: Electron Microscopy service (Ms. Anna Esther Carrillo and Ms. Judith Oro) and Low Temperature and Magnetometry Service (Mr. Bernat Bozzo).

References

View Article Online
DOI: 10.1039/D6NA00067C

[1] Y. Chen, H.A. Zhang and A. El-Ghazaly, *Nanoscale*, 2024, **16**, 8868.
[2] Z. Chai, A. Childress, A.A. Busnaina, *ACS Nano*, 2022, **16**, 17641.
[3] G.M. Whiteside and B. Grzybowski, *Science*, 2002, **295**, 2418.
[4] D. Philp and J.F. Stoddart, *Angew. Chem. Int.*, 1996, **35**, 1154.
[5] L. Abelman, T.A.G. Hageman, P.A. Löthman, M. Mastrangeli and M.C. Elwenspoek, *Sci. Adv.*, 2020, **6**, eabA2007.
[6] K.J.M. Bischop, C.E. Wilmer, S. Soh and B.A. Grzybowski, *Small*, 2009, **5**, 1600.
[7] N. Bowden, A. Terfort, J. Carbeck, G.M. Whitesides, *Science*, 1997, **276**, 233.
[8] J. Labra-Muñoz, Z. Konstantinović, Ll. Balcells, A. Pomar, H.S.J. van der Zant and D. Dulić, *Appl. Phys.Lett.,* 2019, **115**, 063104.
[9] C. Dey, A. Chaudhuri, A. Ghosh and M.M. Goswami, *Chem. Cat. Chem.*, 2017, **9**, 1953.
[10] L. Wu, P.-O. Jubert, D. Berman, W. Imaino, A. Nelson, H. Zhu, S. Zhang and S. Sun, *Nano Lett.*, 2014, **14**, 3395.
[11] E. Myrovali, N. Maniotis, A. Makridis, A. Terzopoulou, V. Ntomprougkidis, K. Simeonidis, D. Sakellari, O. Kalogirou, T. Samaras, R. Salikhov, M. Spasova, M. Farle, U. Wiedwald and M. Angelakeris, *Sci. Rep.*, 2016, **6**, 37934.
[12] M. Rycenga, J.M. McLellan and Y. Xia, *Advanced Materials*, 2008, **20**, 2416.
[13] C. Gatel, F.J. Bonilla, A. Meffre, E. Snoeck, B. Warot-Fonrose, B. Chaudret, L.-M. Lacroix and T. Blon, *Nano Lett.*, 2015, **15**, 6952.
[14] S.M. Taheri, M. Michaelis, T. Friedrich, B. Förster, M. Drechsler, F.M. Römer, P. Bösecke, T. Narayanan, B. Weber, I. Rehberg, S. Rosenfeldt, S. Förster, *PNAS*, 2015, **112**, 14484.
[15] J.G. Donaldson and S.S. Kantorovich, *Nanoscale*, 2015, **7**, 3217.
[16] L. Rossi et al., *Soft Matter*, 2018, **14**, 1080.
[17] Ll. Balcells, I. Stanković, Z. Konstantinović, A. Alagh, V. Fuentes, L. López-Mir, J. Oró, N. Mestres, C. García, A. Pomar and B. Martínez, *Nanoscale*, 2019, **11**, 14194.
[18] H. Yang et alJ, Journal of the American Chemical Society, 2020, **142**, 4438
[19] Y. Chen and A. El-Ghazaly, *Small*, 2023, **19**, 2205079.
[20] M. Varon, M. Beleggia, J. Jordanovic, J. Schiøtz, T. Kasama, V.F. Puntes and C. Frandsen, *Scientific Reports*, 2013, **3**, 1234.
[21] A. Baskin, W.-Y. Lo and P. Kral, *ACS Nano,* 2012, **7**, 6083.
[22] L.T. Hansen, A. Kuhle, A.H. Sorensen, J. Bohr, P.E. Lindelof, *Nanotechnology,* 1998, **9**, 337.
[23] C. Baur, A. Bugacov, B.E. Koel, A. Madhukar, N. Montoya, T.R. Ramachandran, A.A.G. Requicha, R. Resch and P. Will, *Nanotechnology*, 1998, **9**, 360.
[24] A. Rao, E. Gnecco, D. Marchetto, K. Mougin, M. Schonenberger, S. Valeri and E. Meyer, *Nanotechnology*, 2009, **20**, 115706.
[25] D. Dietzel, M. Feldmann, C. Herding, U. D. Schwarz, A. Schirmeisen, *Trib.Lett*., 2010, **39**, 273.
[26] D. Dietzel, T. Monninghoff, L. Jansen, H. Fuchs, C. Ritter, U. D. Schwarz and A. Schirmeisen, *J. Appl. Phys.*, 2007, **102**, 084306.
[27] M. Palacio and B. Bhushan, *Nanotechnology*, 2008, **19**, 315710.
[28] P.E. Sheehan and C. M. Lieber, *Science*, 1996, **272**, 1158.
[29] M.R. Falvo, J. Steele, R. M. Taylor, and R. Superfine, *Phys. Rev. B* 2000, **62**, R10665.
[30] B. Vasić, I. Stanković, A. Matkovic, M. Kratzer, C. Ganser, R. Gajić and C. Teichert, *Nanoscale* 2018, **10**, 18835.
[31] E. Koren, E. Lortscher, C. Rawlings, A.W. Knoll and U. Duerig, *Science* 2015, **348**, 679.
[32] R. Bessler, U. Duerig and E. Koren, *Nano Adv.*, 2019, **1**, 1702.
[33] P. Burger, G. Singh, C. Johansson, C. Moya, G. Bruylants, G. Jakob and A. Kalaboukhov, *ACS Nano*, 2022, **16**, 19253.
[34] Y. Yin, H. Xu, Y. Wang, Z. Liu, S. Zhang, Z. Weng, Z. Song and Z. Wang, *Plasmonics* 2020, **15**, 399.
[35] C.I. Pakes, D.P. George, S. Ramelow, A. Cimmino, D.N. Jamieson and S. Prawer, *J.Magn. Magn. Mater.*, 2004, **272-276**, E1231.
[36] J. Liu, W. Zhang, Y. Li, H. Zhu, R. Qiu, Z. Song, Z. Wang and D. Li, *J.Magn. Magn. Mater.*, 2017, **443**, 184.
[37] M.Z. Atashbar, V.N. Bliznyuk and S. Singamaneni, *Mater. Res. Soc. Symp. Proc*., 2004, **853**, 81.
[38] M. Varenberg, I. Etsion, G. Halperin, *Rev. Sci. Instrum*., 2003, **74**, 3362.
[39] D. Zablotsky, L.L. Rusevich, G. Zvejnieks, V. Kuzovkov, E. Kotomin, *Nanoscale*, 2019, **11**, 7293.
[40] C. Moya, A.M. Abdelgawad, N. Nambiar and S. A. Majetich, *J. Phys. D: Appl. Phys.*, 2017, **50**, 325003.
[41] Israelachvili, Intermolecular and Surface Forces, Academic Press, Boston, p. 253 (2011).
[42] D. Vella, E. du Pontavice, C. L. Hall and A. Goriely, *Proc. R. Soc. A*, 2014, **470**, 20130609.
[43] J. van Herrikhuyzen, R. Willems, S.J. George, C. Flipse, J.C. Gielen, P.C.M. Christianen, A.P.H.J. Schenning and S.C.J. Meskers, Stefan, *ACS Nano*, 2010, **4**, 6501.
[44] S. T. Mehdizadeh, M. Michaelis, T. Friedrich, B. Forster, M. Drechsler, F. M. Romer, P. Bosecke, T. Narayanan, B. Weber, I. Rehberg, S. Rosenfeldt and S. Forster, *PNAS*, 2015, **112**, 14484.
[45] B. Bian, G. Chen, Q. Zheng, J. Du, H. Lu, J.P. Liu, Y. Hu, and Z. Zhang, *Small*, 2018, **14**, 1801184.
[46] D. Dietzel, M. Feldmann, H. Fuchs, U. D. Schwarz, and A. Schirmeisen, *Appl. Phys. Lett*., 2009, **95**, 053104.
[47] J.G. Ku, X.Y. Liu, H.H.Chen, R.D. Deng and Q.X.Yan, AIP Adv., 2016, 6, 025004.
[48] H.M. Lu, W.T. Zheng and Q. Jiang, J. Phys. D Appl. Phys., 2007, 40, 320.
[49] Hans-Jürgen Butt and Michael Kappl, "Surface and Interfacial Forces" WILEY-VCH, 2010.
[50] Gaihuan Ren, Zhanzhao Li, Dongxu Lu, Bo Li, Lulu Ren, Wenwen Di, Hongqin Yu, Jianxin He, and Dejun Sun,

View Article Online
DOI: 10.1039/D6NA00067C

Nanomaterials, 2022, **12**, 2587.

View Article Online
DOI: 10.1039/D6NA00067C

Data for this article, including figures and analysis are available at DIGITAL.CSIC at https://digital.csic.es.